OPEN ACCESS

University of BRISTOL

Calderon, D., Cooper, J., Lowenberg, M., Neild, S., & Coetzee, E. (2019). Sizing High-Aspect-Ratio Wings with a Geometrically Nonlinear Beam Model. *Journal of Aircraft*, *56*(4), 1455-1470. https://doi.org/10.2514/1.C035296

Peer reviewed version

License (if available):
CC BY-NC

Link to published version (if available):
10.2514/1.C035296

Link to publication record in Explore Bristol Research
PDF-document

This is the author accepted manuscript (AAM). The final published version (version of record) is available online via American Institute of Aeronautics and Astronautics at https://arc.aiaa.org/doi/full/10.2514/1.C035296 . Please refer to any applicable terms of use of the publisher.

University of Bristol - Explore Bristol Research
General rights

This document is made available in accordance with publisher policies. Please cite only the published version using the reference above. Full terms of use are available:
http://www.bristol.ac.uk/red/research-policy/pure/user-guides/ebr-terms/

Sizing High Aspect Ratio Wings with a Geometrically Nonlinear Beam Model

D. E. Calderon,* J. E. Cooper,† M. Lowenberg, ‡ and S. A. Neild,§
University of Bristol, Queen's Building, University Walk, Bristol, BS8 1TR, United Kingdom

E. B. Coetzee,¶
Airbus, Filton, Bristol BS34 7PA

This study considers the effect of geometric nonlinearity at the design concept stage of an aircraft wing. A nonlinear finite element beam model adopting the finite volumes concept with an intrinsic strain and curvature formulation is used to size a single-aisle passenger aircraft. A linearised version of this geometrically nonlinear formulation provides a linear benchmark from which the nonlinear predictions of loads, weight and performance can be compared. A baseline study on a wing with an aspect ratio of 18 shows that geometric nonlinearity can have a significant impact on the internal loads, leading to a reduction in the wing weight. The effect of aspect ratio is also explored, yielding optimal values at which the Breguet Range is maximised and showing the effect of geometric nonlinearity on that range. This is complemented by a parameter study on the effect of varying the wing span and surface area, showing that if gate limitations, in the form of span constraints, are imposed on the sizing the optimal aspect ratio is significantly reduced and geometrically nonlinear effects are mitigated. The paper demonstrates the correlation between geometric nonlinearity and the improvements in the wing mass and Breguet range, compared to a conventional linear analysis.

Nomenclature

$\mathcal{A}$	=	Moment arm matrix
A	=	Surface area
A_{str}	=	Stringer area
AR	=	Aspect Ratio
α	=	Trim Angle
b	=	Wing span

*Research Associate, Department of Aerospace Engineering, AIAA Member.
†Royal Academy of Engineering Airbus Sir George White Professor of Aerospace Engineering, FAIAA.
‡Professor of Flight Dynamics, Department of Aerospace Engineering, Senior Member AIAA
§Professor of Nonlinear Dynamics, Department of Civil Engineering.
¶CTO, Airbus Operations Ltd, Pegasus House Aerospace Avenue, Filton, Bristol, BS34 7PA.

BR = Breguet Range

c = Chord length

c_{box} = Wing box chord

c_f = Skin friction coefficient

C_L = Lift coefficient

C_D = Drag coefficient

D = Drag

$\mathcal{D}$ = Global sectional stiffness matrix

δ_e = Elevator deflection

f = Shear offset

$\mathcal{F}$ = External generalised loads

FE = Finite Element

F_x = Axial shear

F_y = Vertical shear

F_z = Fore-aft shear

F_L = Fuselage length

F_D = Fuselage diameter

FF = Form factor

g = Gibbs-Rodriguez rotation parameters

γ = Aerodynamic jig twist

Γ = Circulation

Γ^* = Vortex Strength

h_{sp} = Spar height

HARW = High Aspect Ratio Wing

I = Second moment of area

J = Torsion constant

$\mathcal{K}$ = Global stiffness matrix

l = Bound vortex vector

Λ = Sweep

L = Lift

M_∞ = Mach number

M_p = Pitching moment

M_x = Torque

M_y = In-plane bending moment

M_z = Out-of-plane bending moment

MTOW = Maximum Take-off Weight

N_{str} = Stringer number

OEW = Operating Empty Weight

p = Internal load evaluation points

Ψ = Global strains and curvatures

ρ_{air} = Air density

ρ_{mat} = Material density

q = Displacements

r_g = radius of gyration

S = Surface Area

σ = Direct stress

τ = Shear stress

t = Airfoil thickness

t_{sk} = Skin thickness

t_{sp} = Spar thickness

Θ = Internal generalised forces

U_∞ = Freestream velocity

x = Translational displacements

φ = Rotational displacements

VLM = Vortex Lattice Method

I. Introduction

One of many key factors that determine the viability of a design concept of an aircraft is the cost of manufacturing and operating the aircraft. Given the fact that fuel accounts for a significant portion of the running cost, a key design objective is to minimise fuel burn. With this in mind, many technologies have been developed: laminar flow enablers that include passive [1, 2] or active [3, 4] laminar flow control, supercritical airfoils, vortex generators, carbon fibre composites, slot control and aeroelastic tailoring. Each of these target a particular component of drag. High aspect ratio wings (HARW) aim to reduce the induced drag which is imposed by the presence of tip vortices. This lift induced drag can account for 40% of the aircraft's total drag in cruise [5] and is, therefore, a prime candidate for better fuel

savings and aerodynamic efficiency. The issue however, is that the increase in aspect ratio can have an adverse effect on the root bending moment due to the increase in moment arm of the aerodynamic loading. From a structural point of view, this is undesirable, as it is likely to lead to an increase in mass. A trade-off therefore exists, in which the recovered energy by reducing the induced drag has to be balanced against the required energy to overcome the increase in weight; a multi-disciplinary problem.

Other factors need to be taken into account such as the fuel capacity of the wing. Also, airport design codes, which categorise aircraft predominantly by, but not limited to, wingspan; these are set out by the Federal Aviation Administration (FAA) and the International Civil Aviation Organization (ICAO) limiting certain aircraft to certain airports. One way around this limitation is to add folding wing tips which satisfy these dimensions while folded on the ground, but can be deployed for take-off [6]. As the technologies improve, and environmental initiatives are set, such as Horizon 2020 and Flight Path 2050, HARWs become more appealing to the aircraft manufacturer. There then becomes a need to suitably model HARWs, which tend to be very flexible and consequently the effects of the large geometric deflections on the aerodynamic and structural behaviour need to be considered.

Under these circumstances it is not possible to achieve accurate predictions of the static and dynamic behaviour using conventional linear modelling approaches. In particular, the nonlinear geometric effects on the aerodynamic lift, resulting shear forces and moments, flight mechanics and the 'shortening' of the wing span must be considered using non-conventional approaches. A rich vein of work has recently emerged focusing on the effects of including geometric nonlinearity into the analysis of high aspect ratio wings, and consequently, a number of nonlinear beam formulations have been developed to facilitate this. Developments include displacement-based [7], strain-based [8], intrinsic beam [9] finite element formulations and continuous reduced order models [10]. These studies have highlighted a number of distinctive features of HARWs, such as the strong coupling between structural dynamics and rigid body (flight mechanic) modes [8]. However, little attention has been paid to the effect that such configurations have on the aircraft performance and the resulting structural design.

In this paper, the effect of varying the aspect ratio on the cruise performance, as defined by the Breguet range equation, for a simple flexible aircraft model is examined. Both a traditional linear modelling approach and one that takes non-linear geometric effects into account are considered. The wings are sized based upon equilibrium manoeuvre loads and the aerodynamic jig twist is set such that elliptical loading is achieved in cruise. Once a converged solution is reached, the resulting drag, lift, bending moment, weight and torque distributions are calculated and the cruise range determined using the Breguet equation. A comparison is made between the linear and nonlinear aeroelastic modelling approaches, and conclusions drawn as to the differences that occur in the parameters defining the static aeroelastic behaviour and the 'sweet spot' that reveals the optimal aspect ratio design. Following the AR study, the effects of releasing other parameters such as the wing surface area, are considered to illustrate their impact on the optimal design.

II. Sizing Framework

The sizing framework is based on the premise that the internal structure of the wing can be represented by a beam model and the aerodynamics by a vortex lattice. A similar assumption is found in various aircraft optimisation studies in the literature [11–14]. The internal cross-section of the wingbox is used to evaluate the area, second moment of area and torsional constant and describes the primary mass and stiffness distribution along the wing. These properties are assigned to a series of beam elements that run along the elastic axis of the wing. At the conceptual design stage, avoiding the use of higher fidelity finite element (FE) solvers is hugely beneficial in terms of the computational cost. A 3D FE model of a wing typically has 4 orders of magnitude more states then an 'equivalent' beam model, therefore, unless some form of state reduction is performed, its use in trade studies is limited. Lumped masses are distributed to the nodes in the beam model and represent the secondary, fuel, engine, fuselage and payload masses. The stiffness and mass properties of the model together with the boundary conditions are sufficient to form the structural model. The aerodynamic model is treated using a vortex lattice representation of the lifting surfaces, including its control surfaces. An interpolation scheme based on the infinite plate spline radial basis function allows the transfer of forces and displacements between the aerodynamic model and the structural model and couples the two to form the aeroelastic model. The framework uses this aeroelastic model to evaluate external and internal loads which can be used with the topology of the box section to determine the stresses and hence the required stiffness and mass properties of the beam elements. The imposition of stress constraints with a minimum mass objective drives the sizing of the wing box. A flow diagram describing the sizing process is presented in figure 1.

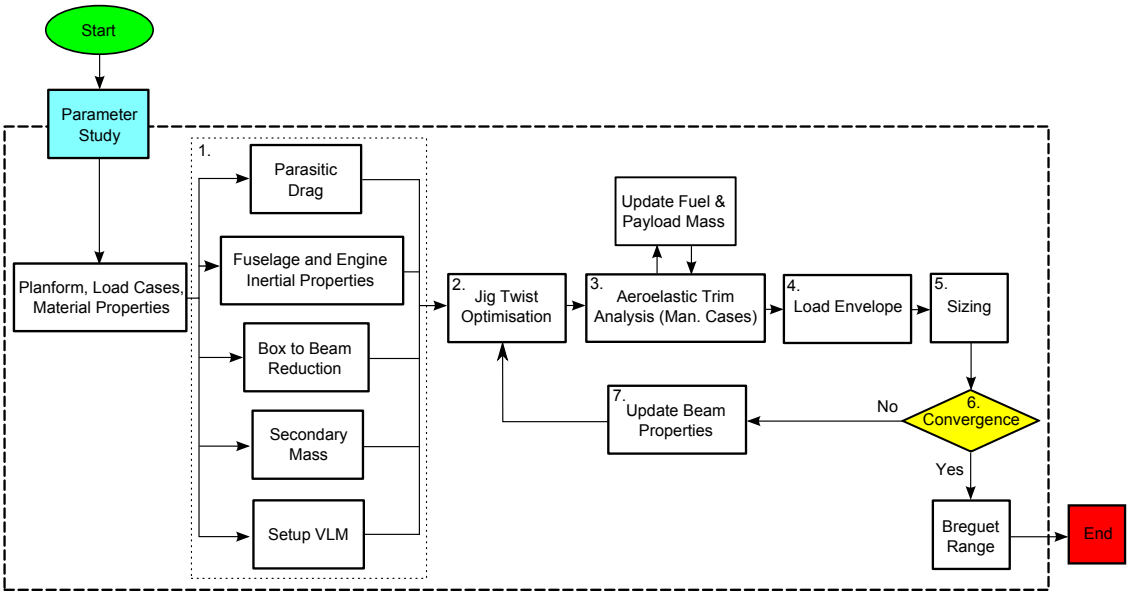

Fig. 1 Flow diagram showing the overall sizing process

Overall the framework performs the following steps: 1. build the aeroelastic model, 2. perform a jig twist

optimisation to achieve on a predefined aerodynamic load distribution, 3. perform an aeroelastic analysis based on the specified load cases, 4. envelope the internal loads, 5. size the internal structure of the wing with the load envelope, 6. check for convergence in mass and 7. if convergence is not found then update the beam properties and repeat 2-6 until convergence is achieved. A parameter study is wrapped around this process to illustrate that inputs to the framework are systematically changed when investigating the effect of certain parameters such as the aspect ratio.

A. Input Definition

The inputs needed to run a sizing are the external geometries of the model, properties of the sizing cases and the material properties. External geometries include the sweep, chord, dihedral and thickness to chord distribution of the lifting surfaces. Airfoil profiles can also be assigned to the lifting surface, to provide camber to the vortex lattice. Engine location is also accepted into the model, described in this case as a fixed distance from the root of the wing. The load case definitions include sufficient information about the flight points such as the altitude and speed as well information about the fuel capacity, payload mass, aircraft center of gravity, load factor and control surface deflections. Material properties include basic properties such as the yield strength, Young's modulus, shear modulus and material density. The following study assumes material isotropy.

B. Box to Beam Reduction

The modelling of the skin, stringers and spars is shown in figure 2. It is assumed that the upper and lower skin thicknesses are equivalent as well as the front and rear spar thicknesses. A similar approach can be found in NeoCASS [15]. The wing box is represented by a rectangular section, the height of which is defined as the mean height at the front and rear spar locations. This approach translates to a reduction factor of 0.79 on the thickness to chord ratio to achieve the box height, based on a NACA 4 series airfoil. Stringers are represented by z-stringers composed of three equivalent segments of length, d, and thickness, $t_{\mathrm{st}} = 0.12d$. The stringer pitch is kept constant, resulting in a variation in stringer number based on the width of the box section. Based on these assumptions it is possible to calculate the properties of each section, such as the second moment of area, torsional constant and cross-sectional area which are then assigned to the 'equivalent' beam model. The skin thickness, t_{sk}, spar thickness, t_{sp} and stringer area, A_{st} for each wing section is initialised before the sizing, allowing the tool to initialise the beam model. Since the sizing routine updates the variables, $(t_{\mathrm{sk}}, t_{\mathrm{sp}}, A_{\mathrm{st}})$, the beam properties have to be re-evaluated at each iteration to estimate the aeroelastic loads in the proceeding loads analysis. The mass distribution based on the aforementioned section properties are referred to as the primary wing mass. Details on the derivations of the section properties are provided in Appendix .A.

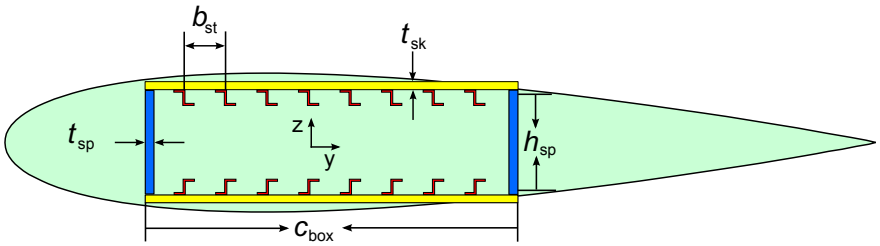

Fig. 2 Cross-section of the wing box used for sizing. The x axis points into the figure.

C. Secondary Masses

The secondary masses, considered here as non-structural masses, are calculated based on the formulae detailed by Torenbeek [16]. These comprise of leading edge and trailing edge sections each with high lift devices. The formulation is provided in Appendix .B for easy reference. The Torenbeek masses are distributed along the wing, and are based on the distribution of its internal volume. The surface area taken up by the type of secondary mass is used to assign a set of lumped masses to each section. These lumped masses are then associated to the nearest beam node with an offset that represents the predicted location of the c.g. of the secondary mass. These offsets ensure a better representation of the inertial properties of the secondary system. During the aeroelastic analysis, the lumped masses are consolidated for performance purposes if they occur on coincident beam nodes.

D. Aeroelastic Model

The aeroelastic model is set up prior to the sizing, based on the initial conditions of the aircraft geometries. The sizing process updates the aeroelastic model by updating the stiffness and mass properties of the beam elements (see figure 1 boxes 5 and 7), however, the resolution of the beam model remains constant as does the location of the beam nodes. In the case of the aerodynamic model, the twist optimisation affects the aerodynamic boundary conditions and not the aerodynamic jig shape. Therefore, in a standalone sizing analysis, the geometry of the wing is fixed and the finite element and aerodynamic mesh is unaltered. More details on how the sizing analysis propagates changes into the aeroelastic model are provided in section II.G. A brief description is provided here on the modelling of the structure and aerodynamics.

1. Structural Model

A finite element model is used to describe the mass and structural properties of the aircraft. A brief description of the underlying beam formulation is provided; more details can be found in the literature [10, 15, 17, 18]. A displacement-based three-node linear/nonlinear finite-volume beam (see figure 3) is implemented. The formulation of this beam model uses the Finite Volumes concept in lieu of variational principles. It was originally proposed by Masarati and Mantegazza [19] and then extended by Ghiringelli *et al.* [17] to nonlinear beams and subsequently other studies. An implementation of the linearised equations can be found in the NeoCASS sizing suite [14, 15]. The formulation is

based on a weighted residuals weak formulation of the finite equilibrium of a beam. It has the benefit of only needing to evaluate the internal loads at two discrete locations along the beam (I and II in figure 3). The node equilibrium equation is

$$\mathcal{F} = \mathcal{A}\mathcal{D}\Psi, \tag{1}$$

where $\mathcal{F}$ is the vector of external loads, $\Psi = \{\epsilon_I, \kappa_I, \epsilon_{II}, \kappa_{II}\}$ is the vector of strains and curvatures in the global reference frame, $\mathcal{D}$ contains the sectional stiffness matrices in the global frame and $\mathcal{A}$ describes the *moment arm* matrix that carries the loads from the evaluation points to the reference points (see figure 3). The strains and curvatures are based on an intrinsic formulation of the beam. A quadratic shape function is used to recover the displacements at the evaluation points along the beam from the three geometric nodes shown in figure 3. This also facilitates the evaluation of the strains and curvatures at these points. It is important to note here that sectional stiffness matrix $\bar{\mathcal{D}}$ is kept constant, and so material nonlinearity is not considered in the study. The notation $(\bar{\cdot})$ refers to a quantity expressed in the local frame. Geometric nonlinearity is introduced through the correct evaluation of the rotation matrices in the node equilibrium equation. For example, the sectional stiffness matrix, $\mathcal{D} = \mathcal{R}\bar{\mathcal{D}}\mathcal{R}^T$, performs a transformation of the strains and curvatures into the local frame and outputs the internal loads in the global frame by pre and post multiplying the local stiffness matrix by the local transformation matrix, $\mathcal{R}$.

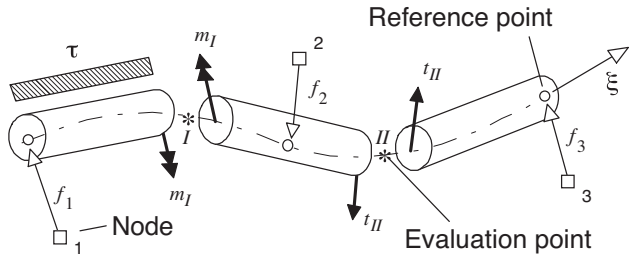

Fig. 3 Three node linear/nonlinear finite volume beam element

The states of the system include the global translational displacements and the updated Gibbs-Rodriguez rotation parameters [17], g. Linearising equation 1 with respect to the structural states generates the structural stiffness matrix, $\mathcal{K}$. In a linear analysis, this is calculated when the beam properties are updated. In a nonlinear analysis, the aircraft structural stiffness is further re-evaluated based on the deformation of the structure.

2. Aerodynamic Model

Aerodynamic forces are calculated using the Vortex Lattice Method (VLM). The method is well documented in the literature; the reader is referred in particular to the description found in Katz and Plotkin [20]. Lifting surfaces are defined by a series of horseshoe vortices that contain collocation points at the 3/4 chord point of each panel. The flow is

assumed to be irrotational, inviscid and incompressible and so the impermeability condition on the surface of the body, is described by $\nabla(\Phi + \Phi_\infty) \cdot \underline{n}$, where, Φ, is the velocity potential. This leads to an expression at the i^{th} collocation point

$$\Big[\sum_{j=1}^{N} (u, v, w)_{i,j} \Gamma_j^* + (U_\infty, V_\infty, W_\infty) \Big] \cdot \underline{n}_i = 0 \tag{2}$$

where $(u, v, w)_{i,j}$ is the induced velocity on the i^{th} collocation point due to the j^{th} vortex line of unit strength, which is determined using the Biot Savart Law. This approach leads to a set of linear algebraic equations equal in number to the collocation points, which in matrix form is

$$w = (\text{AIC})\Gamma^*, \tag{3}$$

where w and AIC are generally referred to as the downwash and Aerodynamic Influence Coefficient matrix, respectively. Here, Γ^*, a column vector of vortex strengths, is the unknown and is recovered by inverting and pre-multiplying by the AIC matrix. The forces are determined using the Kutta Jukowski theorem, so that for each panel

$$\underline{f}_i = \rho_{\text{air}} \underline{U}_\infty \times \Gamma_i^* \underline{l}_i, \tag{4}$$

where $\underline{l}_i$ is the unit vector along the bound vortex of the panel. The resultant force is therefore, perpendicular to the in-flow vector. A symmetry condition at the centerline of the aircraft is easily implemented by reflecting the vortex panels and re-evaluating the AIC matrix on the original collocation points. The AIC for the reflected wing is added to the original AIC so that the updated AIC used in equation 3 becomes

$$\text{AIC} = \text{AIC}_0 + \text{AIC}_{\text{sym}} \tag{5}$$

It is important to note that the control surfaces are treated, not through a physical rotation of the corresponding panels, but instead through a rotation of the unit normals. The same principle is applied to the camber and twist of the undeformed aerodynamic mesh. Allowing for geometric rotations of the control surfaces about its hinge line introduces gaps between nearby panels. This phenomenon in some cases can cause a significant tip effect that can generate spikes in the aerodynamic load distribution, distorting the comparison between the linear and nonlinear analysis. Note that aerodynamic nonlinearity in the form of stall is not considered in this study.

E. Aeroelastic Load Analysis

In this section the linear/nonlinear trim analysis required in both the jig twist optimisation block and the aeroelastic trim analysis block in figure 1 is discussed. The equilibrium manoeuvres described in this paper are symmetric and so the analysis seeks to balance both lift and pitching moment in the process.

1. Linear Analysis

A visual description of the linear trim process is provided in figure 4. In order to perform a linear trim analysis, the aerodynamic forces need to be linearised with respect to the trim variables. A Jacobian consisting of these gradients is used to determine the required pitch, α, and elevator angle, δ_ϵ, needed to trim the aircraft in both lift, L, and pitching moment, M_p, such that

$$\begin{Bmatrix} \Delta\alpha \\ \Delta\delta_\epsilon \end{Bmatrix} = \begin{bmatrix} \frac{\partial L}{\partial \alpha} & \frac{\partial L}{\partial \delta_\epsilon} \\ \frac{\partial M_p}{\partial \alpha} & \frac{\partial M_p}{\partial \delta_\epsilon} \end{bmatrix}^{-1} \begin{Bmatrix} \Delta L \\ \Delta M_p \end{Bmatrix}. \tag{6}$$

where the gradients contain the effects of changes in the structural states, q, which in this case are the 6-axis displacements. The displacements are recovered using the linearised static equilibrium equation so that

$$\Delta q = \left[\frac{\partial F^s_{int}}{\partial q} - \frac{\partial F^s_{aero}}{\partial q} \right]^{-1} \left(\left[\frac{\partial F^s_{aero}}{\partial \alpha} \quad \frac{\partial F^s_{aero}}{\partial \delta_\epsilon} \right] \begin{Bmatrix} \Delta\alpha \\ \Delta\delta_\epsilon \end{Bmatrix} + F^s_{grav} \right) \tag{7}$$

where $\frac{\partial F^s_{int}}{\partial q}$ and $\frac{\partial F^s_{aero}}{\partial q}$, are the structural and aerodynamic stiffness matrices, respectively, $\frac{\partial F^s_{aero}}{\partial \alpha}$ and $\frac{\partial F^s_{aero}}{\partial \delta_\epsilon}$ are the gradients of the aerodynamic loads with respect to the pitch angle and control surface deflection, respectively, and F^s_{grav} is the weight load. The internal loads, F^s_{int}, and aerodynamic loads F^s_{aero}, are recovered using the structural and aerodynamic stiffness matrices. The superscript $(\cdot)^s$ refers to a load expressed at the structural degrees of freedom.

In a linear sizing process, for a given set of beam properties, the gradient matrices relating to the elastic forces in equations 6 and 7 remain constant. The aerodynamic gradient matrices require some modification due to differences in the dynamic pressure at different flight points. It is easy to observe that the linearisation in the linear analysis applies to the entire aeroelastic system and is not confined to the structural system, which is often the case in a typical fluid structure interaction (FSI) process which couples a linear structure with nonlinear aerodynamics.

2. Nonlinear Analysis

In a nonlinear analysis the elastic and external forces are not extrapolated from their linearisation with respect to the structural and aerodynamic trim variables and instead the system must be solved based on the updated states. A flow diagram describing the coupling between the aerodynamic solver and the structural solver in a nonlinear trim analysis is presented in figure 4. The assertion behind the nonlinear trim sequence is that the rigid aircraft can be statically trimmed through a similar process to that described in equation 6. However, a Newton Raphson method is used to ensure that the solution is true upon re-evaluating the aerodynamic loads for those trim variables. It is worth noting at this point that some aerodynamic nonlinearity is introduced through the evaluation of the aerodynamic loads based on the updated trim variables. This process outputs the aerodynamic force distribution which is interpolated onto the

structural model, providing a set of external loads that coincide with the states of the system. The external loads are then applied to the structural system resulting in a deflected model that incorporates geometric nonlinearity. This is achieved by incrementally applying the external load, predicting the displacement using the updated structural stiffness matrix and then evaluating the internal loads with the hope of balancing the equilibrium equation. A Newton Raphson method is used to drive the residual force in the system down to zero, thereby solving the nonlinear static problem at each load increment. At each load step, the displacements at the $(n+1)^{\text{th}}$ sub-iteration are expressed by

$$q_{n+1} = \frac{\partial R_F}{\partial q}^{-1} R_F + q_n, \tag{8}$$

where the residual force, R_F, is the difference between the external and internal loads. The reason why this process is performed in an incremental fashion is to avoid singularities in the Gibbs Rodriguez rotation matrices which involves recovering the rotation parameters from the rotational displacements, φ, using $g = \tan(\varphi/2)$. Therefore, at each load increment, rotational displacements are reset and instead preservation of these displacements is achieved through the update of the local rotation matrices and pre-curvature in the evaluation of the internal loads. This is referred to in the literature as the updated-updated Lagrangian approach [17].

The aerodynamic mesh is then updated based on the new set of structural displacements. The current study uses an infinite plate spline radial basis function used in NeoCASS [15]. The method generates an interpolation matrix which allows the recovery of the aerodynamic mesh from the structural mesh and vice versa; this allows the resolution of the beam model and the aerodynamic mesh to be independent. The deflected aerodynamic mesh is then used in the rigid trim analysis, to determine the new trim variable solution as well as the new aerodynamic loads. The updated aerodynamic loads are then fed to the nonlinear structural solver, to re-evaluate the structural displacements and internal loads. This process is performed iteratively until a convergence is reached based on the norm of the displacements of the model.

3. Jig Twist Optimisation

The sizing process uses an aerodynamic twist optimisation that targets a desired aerodynamic load distribution in cruise. The required loads can be expressed in many forms, for example a local C_l, or a local circulation. In the following study the latter is used to describe an elliptical distribution. The Newton-Raphson method is used to update the twist, γ, such that for the $(k+1)^{\text{th}}$ iteration

$$\gamma^{k+1} = \gamma^k + \Delta\gamma \tag{9}$$

and

$$\Delta\gamma = \left[\frac{\partial\Gamma}{\partial\gamma}\right]^{-1} \Delta\Gamma \tag{10}$$

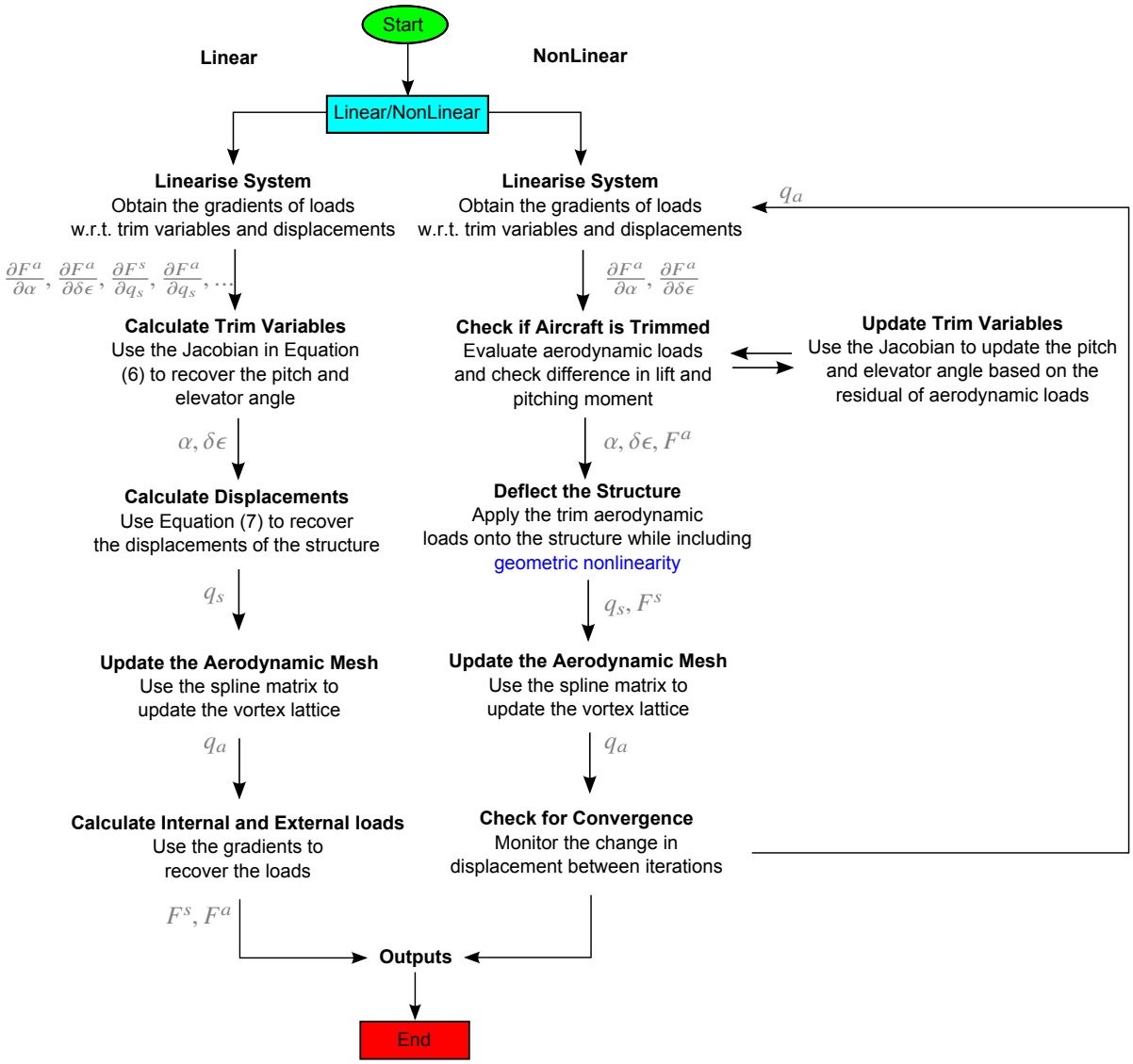

Fig. 4 Aeroelastic trim analysis sequence

Here the target distribution is expressed by $\Gamma = \Gamma_0 f(\theta)$, where Γ_0 is the circulation at the root of the wing and the angle $\theta = \cos^{-1}(2y/b)$ comes from the trigonometric transformation of a point along the wing, y, for a given span, b. The elliptical aerodynamic load distribution is expressed by the relation $f(\theta) = \sin(\theta)$.

For a given circulation distribution, the root circulation is calculated directly for a given root angle and the outboard twist is optimised to attain the target aerodynamic twist. Using this we can express the desired change in circulation as

$$\Gamma_0 f(\theta) - \Gamma^k = \frac{\partial \Gamma}{\partial \gamma} \Delta\gamma \tag{11}$$

where Γ^k is the current circulation. The root circulation is calculated by

$$\Gamma_0 = \frac{\gamma_0 - \gamma + (\frac{\partial \Gamma}{\partial \gamma}^{-1})_{1j}\Gamma^k}{(\frac{\partial \Gamma}{\partial \gamma}^{-1})_{1j} f(\theta)} \tag{12}$$

where the subscripts $(1j)$ refer to the first column of the Jacobian and γ_0 is the desired root twist. At each iteration, the required change in twist is

$$\Delta\gamma = \frac{\partial \Gamma}{\partial \gamma}^{-1} (\Gamma_0 f(\theta) - \Gamma^k). \tag{13}$$

Figure 5 illustrates a comparison between the target distribution and actual distribution generated from the aforementioned process. It can be seen that a good agreement exists between the two.

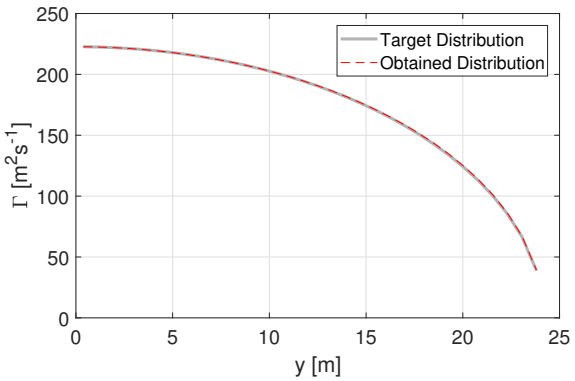

Fig. 5 Circulation vs span showing the target distribution and the obtained distribution

F. Drag Calculations

VLM provides the ability to calculate the induced drag, however, in order to get a good estimation of the L/D and the Breguet Range, it is important to at least estimate the other drag components that are missing from the potential flow method. The component buildup method described by Raymer [21] is used in the following study. The parasitic drag, C_{D_0}, is estimated by summing up the contributions from each component, such as the wing, fuselage and tail. The skin friction drag for each component of the aircraft, C_{f_c}, the form factor FF_c, which takes into account the thickness, and the interference drag factor, Q, which is assumed to be 1.0 in this study, are used in the following summation over all the components

$$C_{D_0} = \sum_c C_{f_c} FF_c Q \frac{S_{wet}}{S_{ref}} \tag{14}$$

where, S_{wet} and S_{ref} are the wetted and reference surface area, respectively. Following Wakayama and Kroo [13] and Kennedy et al, the profile drag, C_{D_p} is calculated using

$$C_{D_p} = C_{D_0} + C_{D_2} C_N^2 \tag{15}$$

where

$$C_{D_2} = \frac{0.38}{\cos^2 \Lambda} C_{D_0} \tag{16}$$

and Λ is the quarter chord sweep. Note that the normal force coefficient, C_N is used instead of C_L, as the latter neglects the sideways components of the aerodynamics forces generated in a nonlinear analysis, where follower forces prevail. Compressibility effects are ignored in this study. The formulae used to predict the skin friction drag and form factor for each component are provided in Appendix .D.

G. Sizing

The purpose of the sizing routine (see box 5 in figure 1) is to determine the thickness of the wing skin, spars and stringers for a set of given loads subject to various constraints, other components of the aircraft such as the empennage and fuselage structural properties remain fixed during this process. The routine uses a gradient based optimisation algorithm implemented in the MATLAB 'fmincon' function. The optimisation routine takes a set of internal loads which consist of an envelope of the various load cases and uses this to determine the stresses in the wing box. A set of 'nonlinear' constraints are devised which need to be satisfied upon finding a minimum mass solution. These constraints ensure that the Von Mises stress in the skin and spar, at ultimate load, does not exceed the yield stress, the skin buckling stress in compression and in shear is not violated, the crippling stresses in the stringers are not violated, and the allowable stress for the string-stringer panel using the Johnson-Euler formulas and the classical Euler equation for the buckling load of a column is also not violated. More detail on the formulations that are used to define the aforementioned constraints is provided in Appendix .C.

The stresses are evaluated using the internal loads generated from the preceeding aeroelastic analysis. Therefore, in this process the section properties are updated using a fixed set of loads. Since the gradient of the aeroelastic loads with respect to the section properties is not included in the optimisation, the sizing sub-routine has to be called a number of times, through an outer iteration loop (see figure 1), allowing the tool to update the beam model with respect to the new sizing variables and re-evaluate the aeroelastic loads outside of the optimisation routine. The advantage of removing the gradient of the aeroelastic loads from the optimisation routine is that it becomes easier to modularise the problem and allow other beam or aerodynamic models to be used in the process. Furthermore, including these gradients require their evaluation, analytically or numerically, which in some cases can be costly.

Once the sub-routine correctly determines the thicknesses of the material in the wing box subject to the stress constraints and minimum mass objective, the thicknesses are then used to update the finite element model. The properties

of each beam element are updated, including its cross sectional area, second moments of area and the torsion constant, so that the only change to the existing aeroelastic model is an update to the beam elements' local sectional stiffness and mass matrix. Updating these matrices, as well as the the global stiffness and mass matrix, only takes place after the sizing sub-routine is finished (see box 7 in figure 1), at which point the aeroelastic trim analysis can be performed on the updated wing box and thus beam model.

In the scope of this study, in which the objective is to minimise wing mass for a set of stress constraints, the approach appeared to be reasonably efficient, requiring between 5 and 10 outer iterations to converge to a sized wing.

H. Breguet Range

A final step in the sizing routine shown in figure 1 is the evaluation of the Breguet Range. The cruise design case is analysed aeroelastically, with half of the mission fuel load. The results are then fed into the Breguet Range formula,

$$\text{Range} = V\Big(\frac{L}{D}\Big)I_{sp}\ln\Big(\frac{W_i}{W_f}\Big), \tag{17}$$

where W_i and W_f are the initial and final weight of the aircraft and $I_{sp} = 1/(0.565hr^{-1})$ is a measure of the propulsive efficiency.

III. Aircraft Model

The 'baseline' model for this study is presented in figure 6. The fuselage and empennage are based on a single-aisle passenger aircraft. For the purpose of this study the baseline wing has an aspect ratio of 18, which, is atypical for this class of aircraft. The lofting surface is presented in figure 6a. The airfoil sections determine the outer geometry of the internal structure and also feed into the prediction of the parasitic drag. Figure 6b represents the aerodynamic mesh. The wings are discretised using 32 spanwise and 8 chordwise panels and the HTP and VTP consist of 5 spanwise by 1 chordwise panel. Aerodynamic panels are not assigned to the fuselage or engine, however, their contribution to the parasitic drag is included in the aircraft drag buildup method described in section II.F. The wing box is shown in figure 6c, from which a finite element model (see 6d) can be generated. The structural model of each wing is represented by 32 beam elements, a series of rigidly connected leading edge and trailing edge nodes and lumped masses. The HTP and VTP each comprise 5 beam elements. The fuselage in this study is treated as a rigid body with translational and rotational inertial properties. The wing to fuselage connection is modeled using a carrythrough boundary condition in which the centreline of the wing is constrained in fore-aft translation, roll and yaw and the root of the wing is constrained in heave, lateral translation and pitch relative to the fuselage node. Overall, the aeroelastic model has 265 aerodynamic panels with 504 structural degrees of freedom.

Key properties of the baseline model are presented in table 1. The wing has a sweep of 12° which is low for a

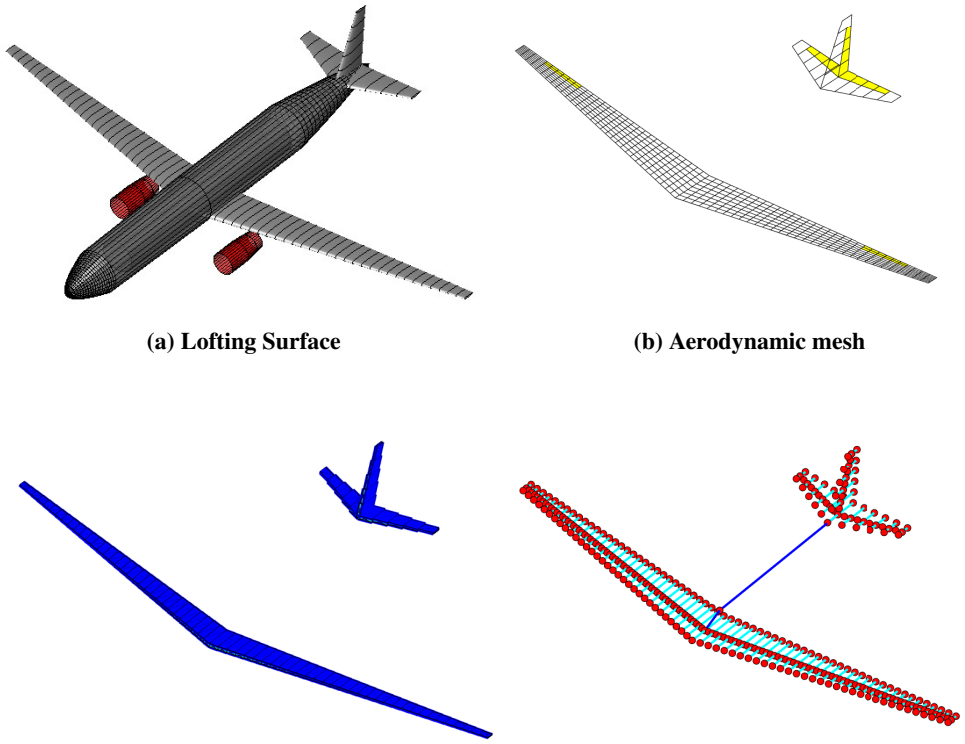

(a) Lofting Surface **(b) Aerodynamic mesh**

(c) Wing box **(d) Finite element model**

Fig. 6 Baseline Model

conventional single-aisle commercial aircraft, however, more typical of that of a high aspect ratio design such as the Boeing SUGAR Volt [22]. The wing has a surface area of $130m^2$, and coincides roughly with that of an Airbus A320 or Boeing 737. The rib pitch, stringer pitch, front and rear spar locations are fixed in the sizing and resemble values of a typical single-aisle passenger aircraft. The engines are placed $5.8m$ from the centerline of the wing and each weigh $3,440kg$. The study assumes that the mass of the aircraft, with the exception of the wing, is kept constant; this is reflected by the Operating Empty Weight (OEW) minus the wing mass shown in table 1. The wing box is built up using an aluminium alloy with a density of $\rho = 2900kg/m^3$, Young's modulus of $E = 68.9$GPa, Poisson's Ratio of 0.33 and yield strength of 276 MPa.

The sizing load cases and design cruise case are listed in table 2. A Mach number of 0.7 is considered to be low compared to a typical commercial short/long haul aircraft. However, its choice is driven by the assumptions of incompressibility used in this study and a 'minimum' speed requirement for this class of aircraft [23]. Note that a symmetric aileron deflection of $-15°$, trailing edge up is introduced to the 2.5g manoeuvre cases for load alleviation purposes. Other types of control surfaces were neglected to simplify parameter studies.

Parameters	Aircraft	Wing	HTP	VTP
Span (m)	-	48.4	11.7	5.9
$\frac{1}{4}c$ Sweep (°)	-	12	20.6	20.6
Taper Ratio	-	0.25	0.35	0.35
Dihedral (°)	-	0	0	0
Half model Surface Area (m^2)	-	65	14	14
Root chord (m)	-	4.3	3.5	3.5
AR	-	18	5	2.5
Root t/c	-	0.13	0.15	0.15
Tip t/c	-	0.09	0.15	0.15
Rib pitch (m)	-	0.60	0.60	0.60
Stringer pitch (m)	-	0.15	0.15	0.15
Front Spar	-	0.15	0.15	0.15
Rear Spar	-	0.65	0.65	0.65
Fuselage length (m)	38.0	-	-	-
Spanwise Engine Location (m)	-	5.8	-	-
Single Engine Mass (kg)	-	3440	-	-
OEW - Wing Mass (kg)	36,000	-	-	-
Fuel Capacity (kg)	16,000	-	-	-
Payload (kg)	18,000	-	-	-

Table 1 Baseline model summary

Load Case	Load Factor	Altitude (m)	Mach No.	Fuel Fraction	Aileron (°)
1	2.5	10000	0.7	1	-15
2	2.5	10000	0.7	0	-15
3	2.5	0	0.4	1	-15
4	2.5	0	0.4	0	-15
5	-1.0	10000	0.7	1	0
6	-1.0	10000	0.7	0	0
7	1.0	10000	0.7	0.5	0

Table 2 Load Cases 1-6 are used for sizing and load case 7 is used for the design cruise case

IV. Baseline Results

In this section the baseline model is sized using linear and geometrically nonlinear beam theory. The two approaches yield two separate models, which have the same external geometry but, due to differences in the evaluation of the loads and displacements, have different internal thicknesses, resulting in different mass and stiffness distributions along the wing. Table 3 summarises key differences in the wings sized using linear and nonlinear analysis. The C_D, C_L, L/D and BR correspond to the aircraft operating at the design cruise (see table 2).

	Linear	Nonlinear	Difference	% Difference
Wing Mass (kg)	15,919	15,127	-792	-5.0
MTOW (kg)	93,881	93,089	-792	-0.8
C_D	0.029	0.028	-0.001	-2.1
C_L	0.653	0.642	-0.09	-1.4
L/D	22.51	22.56	+0.04	+0.2
BR (km)	6,200	6,279	+79	+1.3
Tip Deflection 1g (m)	2.87	3.06	+0.19	+6.7
Tip Deflection max (m)	6.53	6.23	-0.3	-4.6

Table 3 General baseline model (AR = 18) results

Table 3 indicates that the effect of including geometric nonlinearity is a reduction in the wing mass. For this particular configuration the difference is in the region of 5% suggesting that linear beam theory is in this case the conservative approach.

Modelling the geometric nonlinear behaviour of a flexible wing introduces follower forces into the sizing. These appear due to the re-evaluation of loads in trying to balance the system of equations. As the wing deflects, the local aerodynamic/beam frame in which the these loads are evaluated rotate with the structure, and so the orientation of these loads change as a result. This introduces aerodynamic loads which can increasingly contribute to the lateral load and therefore, for a given amount of lift, add circulation to the wing. One can imagine this is undesirable as it is likely to increase the induced drag. Nonetheless Table 3 indicates that the L/D is comparable between the two analyses. The Breguet Range predicted by the nonlinear analysis is more favourable, which can largely be attributed to the reduction in bending moment and hence weight. Figure 7 illustrates the coordinate frames which are used in the evaluation of the loads. In the linear analysis, the local unit vectors that describe the direction of the loads remain unchanged, which is in contrast to the nonlinear analysis.

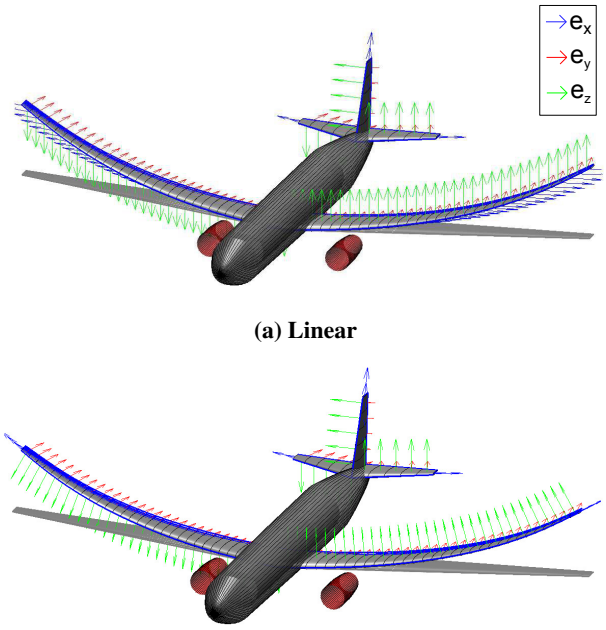

(a) Linear

(b) NonLinear

Fig. 7 Local coordinate frames used to evaluate the loads along the wing for a) linear and b) nonlinear analysis.

Internal load envelopes for the linear and nonlinear sizing are presented in figure 8. The loads shown are the internal loads of the sized wing. The axial shear, in-plane shear and in-plane bending components are noticeably higher when incorporating geometric nonlinearity. Castellani et al.[24] demonstrated a similar effect on an aircraft with AR = 18, using a multibody Finite Segment Approach [25].

This effect can be explained by the effects of linearising the system. The in-plane and axial loads are linearly dependent on the local in-plane ($\bar{\epsilon_y}$) and axial strain ($\bar{\epsilon_x}$) by means of the constitutive law. The linearisation of the node equilibrium equation ensures that in the absence of jig dihedral, these components are dependent on the global in-plane and axial displacements. These load components remain independent of the vertical displacements, leaving the vertical shear force in both the local and global frame solely dependent on the vertical displacement. In terms of the moments, the torque and out-of-plane bending moment become dependent on the curvatures κ_x and κ_y, leaving the in-plane bending moment dependent on κ_z. Linearising the aerodynamic loads with respect to the structural states provides the sensitivity of the lift and pitching moment to the twist of the structure, therefore, external aerodynamic loads are only considered in the global vertical shear F_z and torque M_x, when linearising about the undeformed state. Due to the reasons described earlier on, this implies that in a linear analysis, the load components are predominantly in local vertical shear $\bar{F_z}$, torque $\bar{M_x}$ and out-of-plane bending moment $\bar{M_y}$.

In the case of a geometrically nonlinear system, both the internal and external loads are evaluated about the deformed state. Therefore, the transformation matrix from the global to local frame is frequently updated. Even in the absence

of jig dihedral, considerable axial shear, in-plane shear and in-plane bending moment is observed, as the updated transformation matrix enforces a rotation of the local unit vector e_z, so that global vertical loads can contribute to the axial and in-plane local internal loads. Moreover, the re-evaluation of the aerodynamic loads creates a follower force effect, wherein the contribution to the external loads extends beyond the global vertical and torque components.

The comparison of internal loads between the linear and nonlinear system shows a 4.1% reduction in vertical shear and 5.4% reduction in out-of-plane bending moment using the nonlinear analysis; this agrees well with the difference in wing mass described in table 3. A considerable effect on torque is observed, indicating that the geometrically nonlinear system can in some span locations reduce the torque by as much as 69%. The differences described so far show that accounting for the nonlinear behaviour leads to a reduction in the mass of the wing, however, it also shows that the linear analysis also leads to an underestimate of the axial shear, in-plane shear and in-plane bending moment.

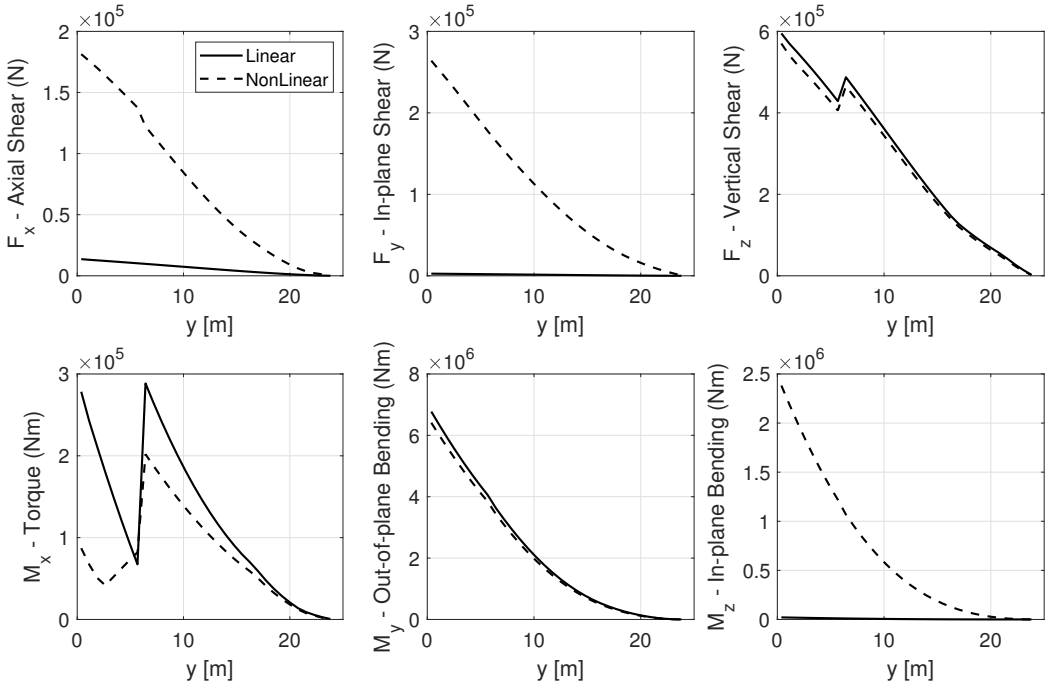

Fig. 8 Internal load envelopes for the linear and nonlinear derived AR = 18 wing

The aerodynamic load distributions for the load cases are presented in figure 9. The drag (c_d), spanwise (c_s) and lift (c_l) components are provided for both the linear and nonlinear analyses. The loads in figure 9 correspond to the sizing cases (load case 1-6) and design cruise case (load case 7) for the final sized wing. For the sizing cases the nonlinear analysis exhibits a reduction in the local lift coefficient towards the tip of the wing. In the case of the spanwise aerodynamic load (c_s), one can observe that the nonlinear system introduces a significant component in this direction. Therefore, despite the fact that the redistribution of the local lift coefficient reduces the root bending moment, the increase in the lateral loads has the opposite effect.

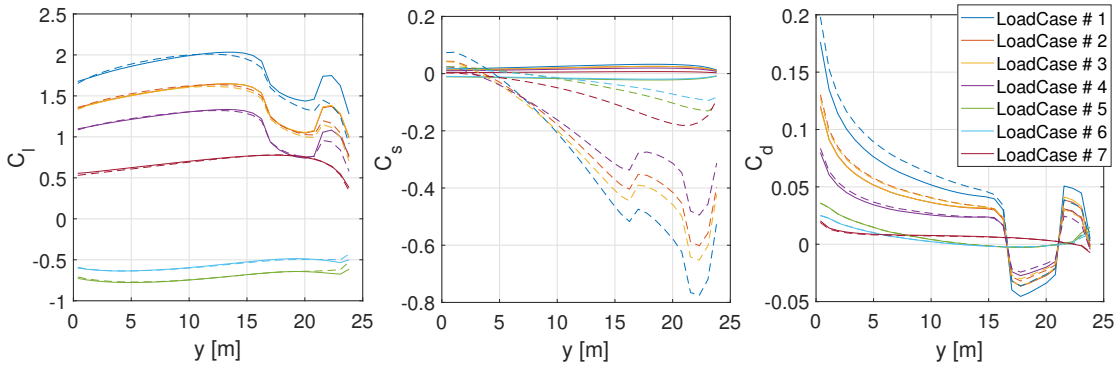

Fig. 9 Aerodynamic load coefficients for the linear and nonlinear derived AR = 18 wing. Solid and dashed lines correspond to the linear and nonlinear analysis, respectively.

The effect of reducing the internal loads through the integration of geometric nonlinearity in the sizing process is the ability to remove mass from the structure while still satisfying the constraints defined in section II.G. Figure 10 illustrates the change in stiffness properties along the wing between linear and nonlinear analysis and confirms that the wing sized using nonlinear analysis is in fact more flexible than the linear wing, in fore-aft bending, out-of plane bending and torsional stiffness.

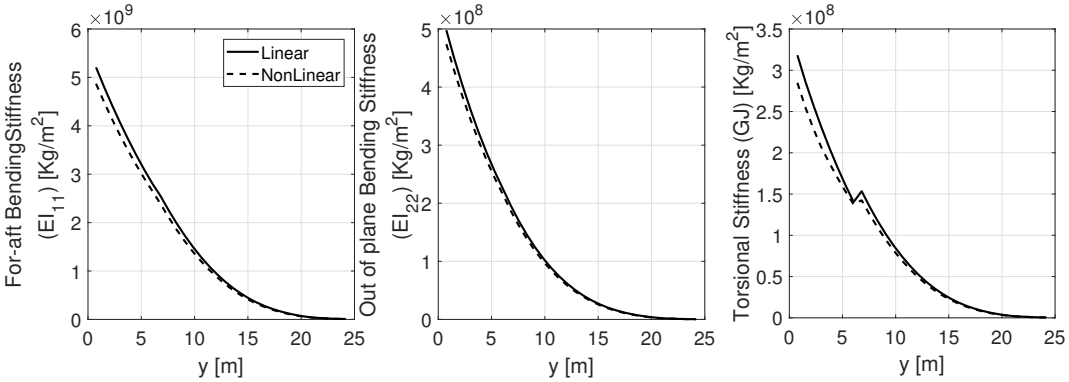

Fig. 10 Axial, bending and torsional stiffness of the linear and nonlinear derived AR = 18 wing

V. AR Study

This section considers the effect of changing the aspect ratio on the sizing and performance of the aircraft for the wing treated both with a linear analysis (the 'linear wing') and a nonlinear analysis (the 'nonlinear wing'). An assumption is made here that the change in aspect ratio is achieved by increasing the span and reducing the root chord. The sweep, taper, dihedral and surface area remain unchanged. Figure 11 illustrates the change in wing planform with AR for values of 10 to 24 in intervals of 2. The wing reference point which is defined as the root beam location point, is kept constant upon changing the aspect ratio. Notice also that the engine location is defined in absolute space. The center of gravity of the aircraft is also fixed at 15% of the mean aerodynamic chord.

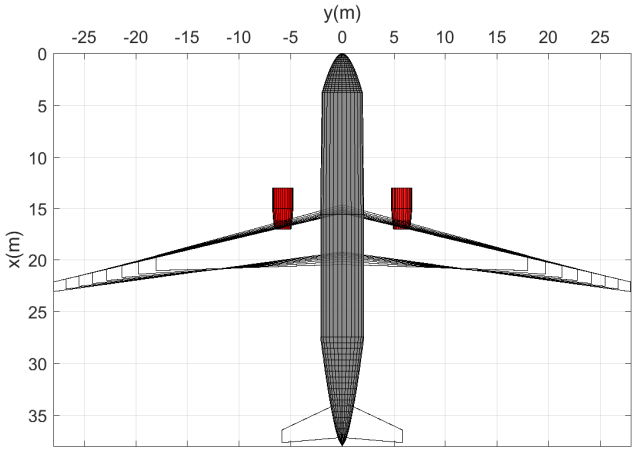

Fig. 11 Wing geometry vs AR

A parameter study is performed, where for each aspect ratio the wing is sized twice, once with the linear analysis and once with the nonlinear. It is important to note here that the AR is not a variable within an individual sizing analysis but instead a pre-defined property of the wing which is systematically defined as an input to a new sizing (see figure 1). Therefore, the parameter study is the result of multiple sizing processes such that, in each of them, the wing planform is fixed. The effect this has on the mass, L/D and Breguet Range is shown in figure 12.

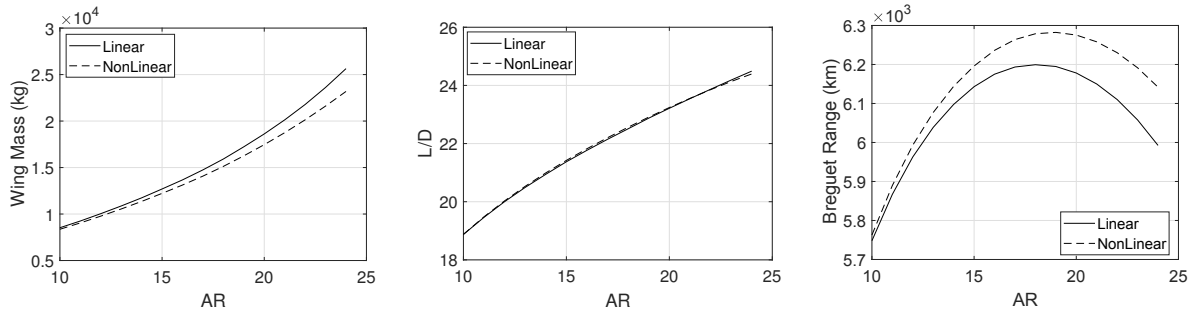

(a) Wing mass **(b) L/D** **(c) Breguet Range**

Fig. 12 a) Wing mass, b) L/D and c) Breguet Range for AR = 10:2:24 for the linear and nonlinear analysis

Figure 12a illustrates the adverse effect of increasing the aspect ratio on the mass of the wing. Furthermore, it also shows that with increasing aspect ratio the difference between the linear and nonlinear wing increases. The difference in wing mass is in the region of 5% for AR = 18; this reduces to 1.4% for AR = 10 and increases to 12.5% for AR = 24. Therefore, the inherent load alleviation properties of including geometric nonlinearity into the trim analysis, which predominantly occurs in out-of-plane bending, contributes to a lower wing weight when compared to the outcome of a sizing that relies on linear aeroelastic analysis.

The effect of aspect ratio on the L/D is shown in figure 12b, demonstrating that the improvements increasing the AR

has on the aerodynamic performance of the wing. It is interesting to see that the effect of geometric nonlinearity, here, is imperceptible. This result is perhaps surprising, as one might expect that for a given lift, the nonlinear analysis would incur greater drag due to the additional components of the aerodynamic force arising from the follower force effect.

In order to take into account both the aerodynamic and structural efficiency we consider the Breguet Range. The results are presented in figure 12c. An optimal AR is observed for the wing sized using linear analysis and the wing sized using the nonlinear one, occurs at AR = 18 and 19 respectively. Moreover, the Breguet Range is improved for the nonlinear wing. The improvement is a consequence of the mass reduction experienced when including geometric nonlinearity in the wing modelling.

Certainly, the aspect ratio values shown here are high for a single-aisle passenger aircraft which are generally in the region of AR $\approx$ 9. However, it is important to emphasise that the values are the result of an unconstrained analysis on the wing span, where the objective is to minimise the mass and the Breguet Range is a by-product of the sizing. Therefore, no constraints have been placed on the design of the wings to satisfy airport gate requirements, which are in fact considered in Sec VI. The analysis indicates that by increasing the aspect ratio from 10 to the suggested optimal aspect ratio of 18, the Breguet Range may increase by 13%, however, the wing mass increases by almost 140%. Therefore, in reality the optimal aspect ratio, in a more encompassing cost function, which includes manufacturing, direct operating and maintenance costs, is likely to be lower. What is interesting here is that if it became viable to design higher aspect ratio wings, the lack of geometric nonlinearity in the design concept stage could potentially lead to errors in the calculation of the loads, the wing mass and the optimal design.

Figure 13 presents the lift distribution along the wing for aspect ratios of 10, 18 and 24. The differences between the linear and nonlinear analysis are more noticeable with higher aspect ratios. The nonlinear analysis redistributes the aerodynamic load so that more of the lift is shifted inboard, which helps to alleviate the loads.

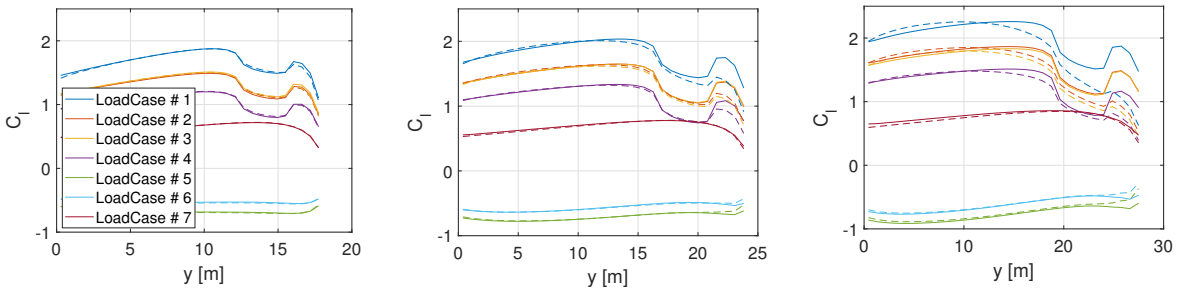

(a) AR = 10 **(b) AR = 18** **(c) AR = 24**

Fig. 13 Local lift coefficient along the wing for a) AR = 10, b) AR = 18 and c) AR = 24. Solid lines are linear and dashed lines are nonlinear.

Figure 14 provides an envelope of the tip displacements and tip rotations, about the global x-axis, consisting of the maximum and minimum values exhibited across all of the maneuver cases, as well as the values achieved in cruise. This

is presented for a range of aspect ratios, with and without geometric nonlinearity. While the influence of the nonlinearity is described here as a function of the aspect ratio, note that it is strongly dependent on the flexibility of the structure. Geometric nonlinearity exists in large displacements and rotations, and therefore, an over-sized, stiffer high aspect ratio wing will exercise this to a lesser extent. Figure 14 confirms that changing the aspect ratio has a significant impact on the relative tip displacement and tip rotation. The displacements vary from 6.1% to 21.3% of the span and the spanwise tip rotation vary from 15° to 55° for AR = 10 to 24. This gives an insight into the degree of displacement and rotation required to generate differences between the linear and nonlinear analysis. For example, if one defines the requirement for nonlinear analysis to be when the nonlinearity accounts for a change in mass of more than 3% then, based on the current configuration, it is required if the tip displacement exceeds 9% of the span or if the spanwise tip rotation exceeds 21°. Figure 14 indicates that this corresponds to an aspect ratio of 13.5.

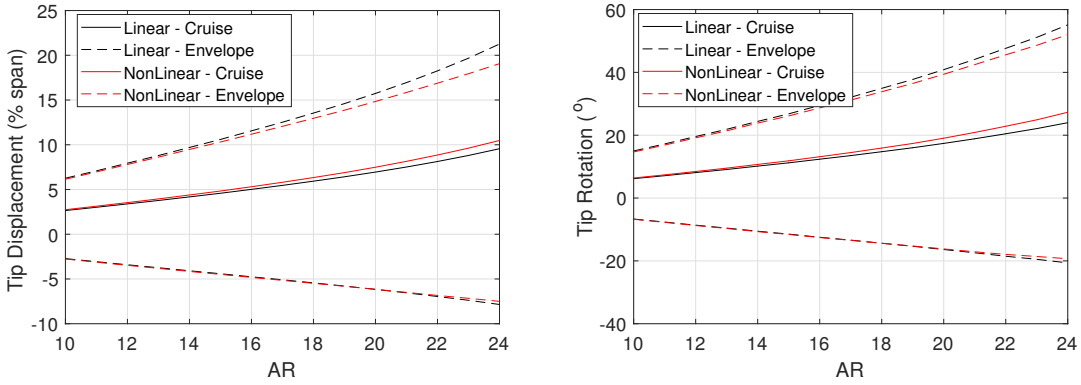

(a) Tip displacement **(b) Tip rotation**

Fig. 14 Wing a) tip displacement and b) tip rotation against AR for each loadcase, comparing linear and nonlinear analysis.

VI. Sensitivity Study

The paper has so far considered the effects of geometric nonlinearity on the sizing and performance of a baseline wing. The aspect ratio of that wing is varied while maintaining constant surface area. In this section, the variation of other wing parameters such as the wing surface area is considered to give an indication of the sensitivity of interesting quantities such as the wing mass and Breguet range to these parameters.

A. Wing Surface Area

An important consideration in designing the wing of a commercial aircraft is its airport aircraft design code. The ICAO/FAA codes primarily classify an aircraft based on its wing span. Airports have an aircraft capacity based on these codes, which enforces restrictions on the dimensions of the aircraft to facilitate taxiing and gate parking. Therefore, in some instances, the wing span can form a constraint in the design of the wing. For example, an Airbus A320 and the

Boeing 737 are both considered to be group III aircraft under the FAA regulations, wherein their wing span is less then 36m. With this in mind it is important to consider the effects of these constraints on the presented study.

Figure 15 compares the Breguet Range and wing mass for various combinations of wing surface area and span and is presented for both linear (figures 15a and 15c) and nonlinear analysis (figures 15b and 15d). Figures 15a and 15b compare the Breguet Range, which is represented by the coloured contour plot. Dashed lines indicate the aspect ratio for a particular combination of area and span. The results generated in figure 12c can be recovered by tracing the Breguet Range along the contour, for a wing area of $130m^2$. In doing so, the optimal aspect ratios, with respect to the Breguet Range, are 18 and 19, respectively, for the linear and nonlinear analysis.

Firstly, the difference between the linear and nonlinear analysis increases with higher aspect ratios. Secondly, the contours indicate there is some benefit in increasing the wing surface area to $145m^2$ from the baseline configuration of $130m^2$ for better Breguet Range.

Line plots are also superposed on the contours to indicate the effect of fixing the wing surface area or the wing span, on the optimal aspect ratio with respect to Breguet Range. The blue markers, indicate that as the wing span is systematically fixed to higher values, the optimal aspect ratio increases. It is interesting to note here that in the case of a span restriction of 36 m, the optimal aspect ratio is 11.6, which is significantly lower than what was observed with the baseline model. The red markers indicate that if the wing surface area is fixed and the wing span is released, the optimal aspect ratio is largely unaffected. A consistent value of AR = 18 is observed for the linear case, and a value of AR = 19 is observed for the nonlinear.

The wing mass is investigated in figures 15c and 15d. Similarly to the baseline model, a strong correlation exists between the aspect ratio and the mass of the wing. Furthermore, the difference between the linear and nonlinear analysis increases with higher aspect ratio. Line plots are superposed on the wing mass contour plots in a similar manner to those found on the Breguet Range plot. Red markers indicate that minimum mass is achieved at the lower bound of the wing span parameter space considered in this study for fixed wing surface area. The blue markers on the other hand indicate that if the wing span is fixed in the sizing, the optimal wing surface area for minimum mass increases as the assumption of wing span increases. It is interesting to observe that for a wing span of 36 m, the optimal aspect ratio for minimum mass is AR = 9.4 for the linear analysis, which is significantly closer to a conventional single aisle passenger aircraft; this is marginally higher for the nonlinear analysis.

B. Discussion

Figure 16 summarises the effects of geometric nonlinearity by comparing the percentage difference in wing mass, bending moment, L/D and Breguet range between the linear and nonlinear analyses. The data set corresponds to the wing area vs span parameter study provided in section VI.A. Each data point consists of a comparison between the geometrically linear and geometrically nonlinear sizing routines, where a positive value indicates a reduction in that

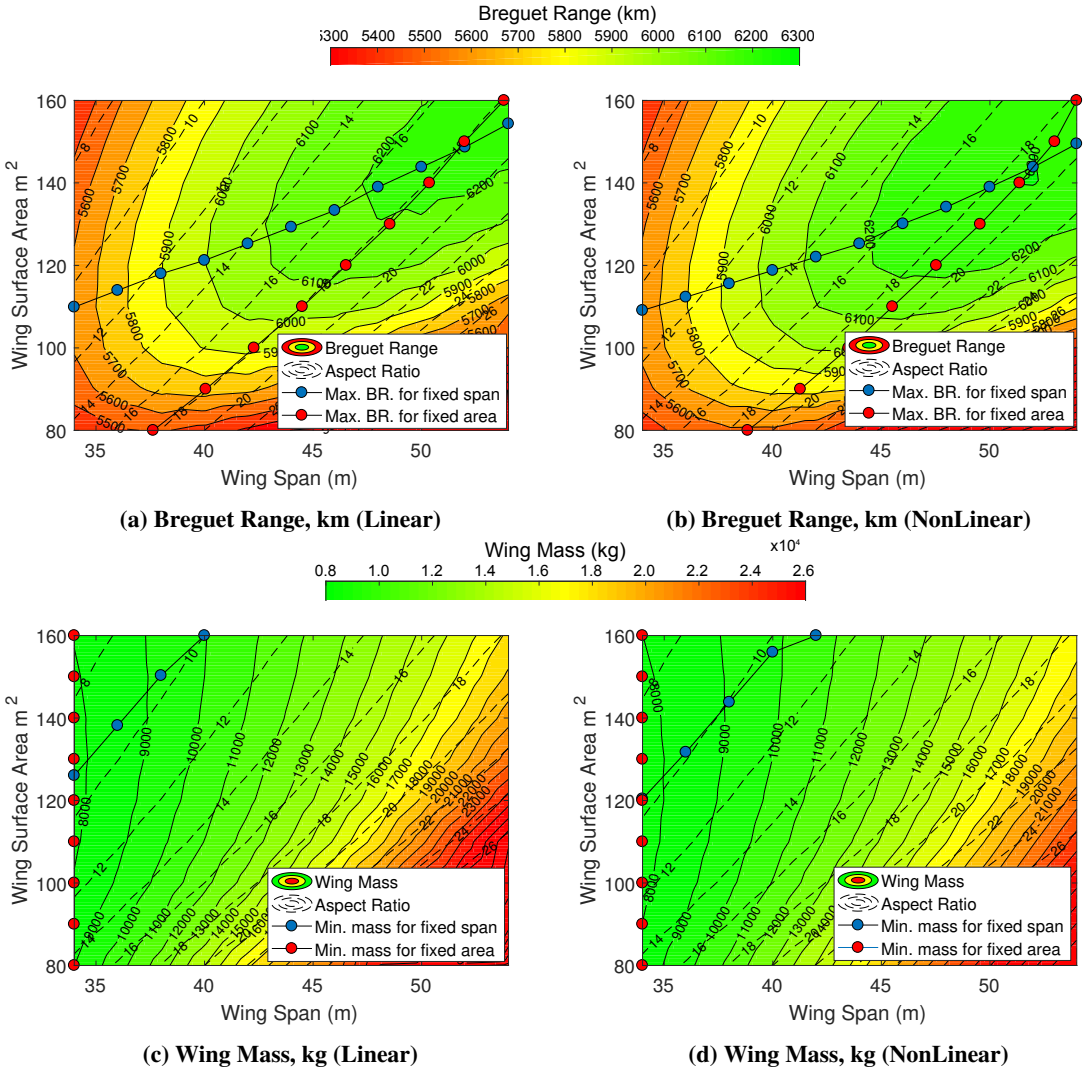

(a) Breguet Range, km (Linear)

(b) Breguet Range, km (NonLinear)

(c) Wing Mass, kg (Linear)

(d) Wing Mass, kg (NonLinear)

Fig. 15 Parameter sweep of the wing surface area and wing span

quantity due to geometric nonlinearity. The difference is displayed against tip displacement as a percentage of wing span.

Figure 16a compares the effects geometric nonlinearity have on the wing mass. One can see that for a range of wing planforms the effect is a reduction in the mass. Comparing the baseline model, which is represented by the green marker in each of the plots in figure 16, with other models of similar tip displacement, indicates that the difference in mass between the linear and nonlinear analysis ranges from 3.8% to 8.5%. The bending moment is also mitigated by including the effects of geometric nonlinearity which is shown in 16b. In the case of the aerodynamic efficiency (see figure 16c), the effects are less clear, typically showing differences of within 1%. Figure 16d shows a strong correlation between the tip displacement and the difference in the Breguet range; in all cases the Breguet range performance prediction is improved by including geometrically nonlinear effects.

The benefit of consolidating comparisons in such a fashion is in the ability to give the designer an indication of the differences the inclusion of geometric nonlinearity in the modelling will have on the quantities such as the mass, using information that may already exist based on a linear analysis. Evidently the results presented here indicate that the tip displacement as a percentage of span can give an indication of the effect of geometric nonlinearity. This of course is to be expected since geometric nonlinearity is a by product of large deformations.

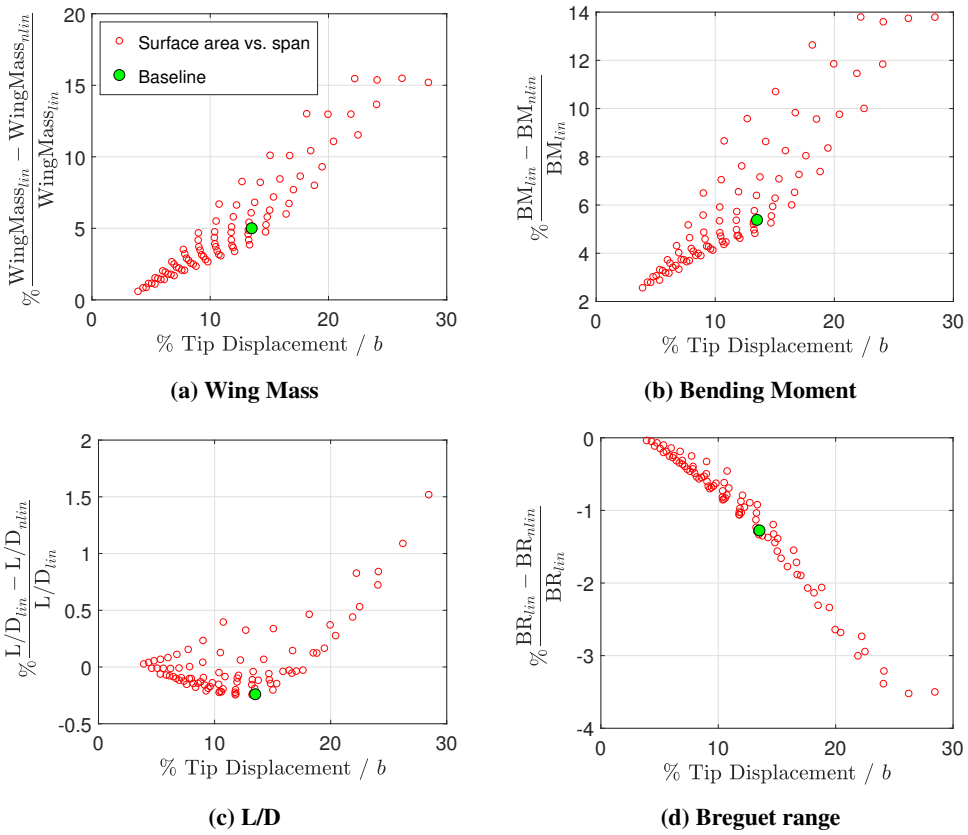

(a) Wing Mass **(b) Bending Moment**

(c) L/D **(d) Breguet range**

Fig. 16 Scatter plots comparing the percentage difference in a) wing mass, b) bending moment, c) L/D and d) Breguet range between linear and nonlinear analysis, relative to the maximum tip displacement, with various assumptions of span and surface area.

VII. Conclusions

In this paper a displacement-based finite element method using the finite volumes approach is used to incorporate geometric nonlinearity into the sizing of a wing. A moderately swept back, straight tapered wing is sized based on the loads extracted from a linear or nonlinear trim analysis. The loads together with a gradient based optimisation routine, with constraints based on the material and buckling stress allowables, are used to size the beam-box sections of the wing.

Results from the baseline model with an aspect ratio of 18 indicate that correctly modelling the large deflections and the nonlinear follower forces, from the accompanying aerodynamic solver, can lead to a reduction in wing mass of over

5%. It is also observed that using a linear analysis leads to a slight overestimate of the aerodynamic efficiency . The reduction in mass results from a redistribution of the aerodynamic loading that favourably reduces the root bending moment. Axial shear, in-plane shear and in-plane bending are adversely affected by geometric nonlinearity, however, not enough to prevent the nonlinear analysis from generating a lighter more flexible wing.

The effect of varying the aspect ratio of the baseline wing is studied, showing that optimum aspect ratio differs depending on whether or not geometric nonlinearity is taken into account in the sizing process. Including the nonlinear behaviour increases the predicted optimum value to 19 from a value of 18 which is found for a linear analysis. This result is largely attributed to the overprediction of sizing loads in the linear analysis, which increases the structural wing mass over the nonlinear approach.

A study is carried out on the effect of obtaining different aspect ratios through various combinations of wing surface area and wing span. In doing so, it is shown that the optimal aspect ratio is significantly reduced to 11.6 while satisfying the FAA group III design code of 36 m wing span. This is reduced even further if the optimum is defined by minimum mass, aligning the design with conventional aircraft. Overall, the effects of geometric nonlinearity are more pronounced on wings with higher aspect ratios, however, the effects of nonlinearity are better correlated against the tip displacement as a percentage of span. A strong correlation is shown between the tip displacement exhibited by the wing and the reduction in the wing mass due to geometric nonlinearity; the same is shown for the improvement in the the Breguet range. In the case of the aerodynamic efficiency, L/D, the correlation between tip displacement and therefore, the effect of geometric nonlinearity appears to be less clear.

Appendix

A. Section Properties

The second moment of area, $I_{yy}^{\mathrm{st}_j}$, of an individual stringer about the the centroid of the box section is expressed by

$$I_{yy}^{\mathrm{st}} = d^4\left(\frac{2}{3}d_s^3 + d_s^2 + \frac{7}{12}d_s\right) + A_{\mathrm{st}}\left(\frac{h_{\mathrm{sp}}}{2} - t_{\mathrm{sk}} - \left(\frac{d}{2} + d_s d\right)^2\right) \tag{18}$$

where $d_s = 0.12$ is the thickness to length ratio of the stringer segments. After some manipulation, the second moment of area, I_{zz}^{st}, of the j^{th} stringer, about its own centroid is expressed as

$$I_{zz}^{\mathrm{st}_j} = \frac{d^4}{2}\left(\frac{4d_s}{3} + \frac{d_s^3}{6}\right). \tag{19}$$

The stringers are distributed evenly along the skin of the box and so the second moment of area of all the stringers about the centroid of the box is expressed by

$$I_{zz}^{\text{st}} = 2\sum_{j=1}^{N_{\text{st}}}(\frac{c_{\text{box}}}{2} - j\frac{c_{\text{box}}}{N_{\text{st}}+1})^2 A_{\text{st}} + I_{zz}^{\text{st}_j}), \tag{20}$$

where N_{st} refers to the number of stringers for a particular section, which can also be expressed as

$$I_{zz}^{\text{st}} = 2(N_{\text{st}} I_{zz}^{\text{st}_j} + A_{\text{st}} c_{\text{box}}^2 N_{\text{st}}(-\frac{1}{4} + \frac{N_{\text{st}}+1/2}{3(N_{\text{st}}+1)})). \tag{21}$$

The overall second moments of area of the box section are then defined as:

$$I_{yy} = N_{\text{st}} I_{yy}^{\text{st}} + \frac{1}{12}(c_{box}(h_{\text{sp}} + 2t_{\text{sk}})^3 - (c_{\text{box}} - 2t_{\text{sp}})(h_{\text{sp}})^3) \tag{22}$$

$$I_{zz} = I_{zz}^{\text{st}} + \frac{1}{12}((h_{\text{sp}} + 2t_{\text{sk}})c_{\text{box}}^3 - (h_{\text{sp}})(c_{\text{box}} - 2t_{\text{sp}})^3) \tag{23}$$

$$I_{zy} = 2N_{\text{st}} t_{st} d \tag{24}$$

The torsion constant, J, for thin walled tubes is given by

$$J = \frac{4(h_{\text{sp}} + t_{\text{sk}})^2 (C_{\text{box}} - t_{\text{sp}})^2}{2(\frac{h_{\text{sp}}+t_{\text{sk}}}{t_{\text{sp}}} + \frac{C_{\text{box}}-t_{\text{sp}}}{t_{\text{sk}}})} \tag{25}$$

B. Secondary Masses

The formulae used from Torenbeek [16] to represent the secondary masses are as follows. Note that W and S are the component weight and surface area.

1. Fixed leading edges

$$W_{fle}/S_{fle} = 75 * 1.4\left(1 + \sqrt{MTOW/10^6}\right) \tag{26}$$

2. Trailing edges

$$W_{fte}/S_{fte} = 60\left(1 + 1.6\sqrt{MTOW/10^6}\right) \tag{27}$$

3. Leading edge high lift devices

$$W_{slat}/S_{slat} = 160\left(1 + 0.7\sqrt{MTOW/10^6}\right) \tag{28}$$

4. Trailing edge high lift devices

$$W_{tef}/S_{tef} = 100\left(1 + \sqrt{MTOW/10^6}\right) \tag{29}$$

5. Ailerons

$$W_a/S_a = 125\left(1 + 0.5\left(MTOW/10^6\right)^{1/4}\right) \tag{30}$$

C. Sizing Constraints

1. Material Strength

The bending stresses on the top and bottom covers and the spars are determined by

$$\begin{aligned} \sigma_{\text{sk}} &= \left(\frac{h_{\text{sp}}}{2} - \frac{t_{\text{sk}}}{2}\right)\frac{M_y}{I_{yy}}, \\ \sigma_{\text{sp}} &= \left(\frac{c_{\text{box}}}{2} - \frac{t_{\text{sp}}}{2}\right)\frac{M_z}{I_{zz}}. \end{aligned} \tag{31}$$

where h_{sp} is the spar height, t_{sk} is the skin thickness, t_{sp} is the spar thickness and c_{box} is the chord of the box. The shear stress is evaluated by

$$\begin{aligned} \tau_{\text{sk}} &= \frac{M_x}{2\Omega t_{\text{sk}}} + \frac{F_y}{2c_{\text{box}}t_{\text{sk}}} + 0.5\frac{F_z}{2h_{\text{sp}}t_{sk}}, \\ \tau_{\text{sp}} &= \frac{M_x}{2\Omega t_{\text{sp}}} + \frac{F_z}{2h_{sp}t_{\text{sp}}} + 0.25\frac{F_y}{2c_{\text{box}}t_{\text{sp}}}. \end{aligned} \tag{32}$$

where Ω is the area enclosed by the mean line along the skin and spar.

The shear and bending stresses are then combined in a von Mises Yield Criterion which is determined by

$$\begin{aligned} \sigma^v_{\text{sk}} &= \sqrt{\sigma^2_{\text{sk}} + 3\tau^2_{\text{sk}}}, \\ \sigma^v_{\text{sp}} &= \sqrt{\sigma^2_{\text{sp}} + 3\tau^2_{\text{sp}}}. \end{aligned} \tag{33}$$

so that the constraints for the sizing become

$$\begin{aligned} \frac{\sigma^{v}_{\mathrm{sk}}}{\sigma_{yield}} &\leq 1, \\ \frac{\sigma^{v}_{\mathrm{sp}}}{\sigma_{yield}} &\leq 1 \end{aligned} \tag{34}$$

where σ_{yield} is the yield stress of the material.

2. Skin Buckling

The buckling stress of the skin is given by

$$\sigma_{\mathrm{sk}_b} = \frac{k_c \pi^2 E}{12(1-\upsilon^2)}\left(\frac{t_{\mathrm{sk}}}{b_{st}}\right)^2, k_c = 4 \tag{35}$$

$$\tau_{\mathrm{sk}_b} = \frac{k_s \pi^2 E}{12(1-\upsilon^2)}\left(\frac{t_{\mathrm{sk}}}{b_{st}}\right)^2, k_s = 5.6 \tag{36}$$

where, k_c and k_s are the compression and shear buckling coefficients, υ is the poisson's ratio and b_{st} is the stringer pitch. The principle stress formulation is used to provide the sizing with a skin buckling constraint.

$$\sigma_p = 1 - \frac{2}{\frac{\sigma_{\mathrm{sk}_b}}{\sigma_{cr}} + \sqrt{\frac{\sigma_{sk_b}}{\sigma_{cr}}^2 + 4\frac{\tau_{\mathrm{sk}_b}}{\tau_{cr}}^2}} \leq 1 \tag{37}$$

3. Skin-Stringer Failure

The non-dimensional crippling stress for the individual segments of the stringers is expressed by Niu [26] as

$$\frac{\sigma^{*}_{cc}}{\sigma_{all}} = B\left(\sqrt{\frac{\sigma_{all}}{E}}\left(\frac{d}{t_{st}}\right)\right)^{A} \tag{38}$$

where σ_{all} is the allowable stress and the coefficients A and B are given by

$$\left.\begin{aligned} A &= -0.7885, \\ B &= 0.6194, \end{aligned}\right\} \text{One free edge} \tag{39}$$

$$\left.\begin{aligned} A &= -0.8046, \\ B &= 1.2117, \end{aligned}\right\} \text{No free edge} \tag{40}$$

The cut-off stress is implemented so that the non-dimensional crippling stress becomes

$$\frac{\sigma_{cc}}{\sigma_{all}} = \min(\frac{\sigma^*_{cc}}{\sigma_{all}}, 1.45) \tag{41}$$

The crippling stress for the entire stringer is then determined by a weighted average of the crippling stress of the segments, so that

$$\sigma_{cc} = \frac{\sum d_n t_{st_n} \sigma_{cc_n}}{\sum d_n t_{st_n}} \tag{42}$$

where the subscript n refers to the 3 segments of the stringer.

The effective width of the skin-stringer panel is determined by

$$w_{eff} = 1.7 t_{\mathrm{sk}} \sqrt{\frac{E}{\sigma_{st}}} \tag{43}$$

and the effective area follows from

$$A_{eff} = w_{eff} t_{\mathrm{sk}}. \tag{44}$$

The radius of gyration is

$$r_g = \sqrt{\frac{I}{A_{st} + A_{eff}}} \tag{45}$$

and the slenderness ratio is

$$K = \frac{L}{r_g \sqrt{c}} \tag{46}$$

A critical slenderness ratio is determined from the crippling stress

$$K_{cr} = \pi \sqrt{\frac{2E}{\sigma_{cc}}} \tag{47}$$

The allowable column stress is then determined through the classical Euler equation or the Johnson-Euler formula, respectively,

$$\begin{aligned} \sigma_c &= \sigma_{cc}\left(1 - \frac{\sigma_{cc} K^2}{4\pi^2 E}\right), && \text{for } K \le K_{cr} \\ \sigma_c &= \frac{\pi^2 E}{K^2}, && \text{for } K > K_{cr} \end{aligned} \tag{48}$$

The constraint used in the sizing can then be expressed as

$$\frac{\sigma_{st}}{\sigma_c} \leq 1 \tag{49}$$

D. Drag Calculations

The calculation of the skin friction coefficient, C_{f_c}, is based on the theory described by Raymer [21] and is performed by estimating the portion of the airfoil experiencing laminar and turbulent flow. Assuming a critical Reynolds' number of $Re_{\text{cr}} = 1 \times 10^6$, we can estimate the point of transition from laminar to turbulent flow by

$$x_{\text{cr}} = \frac{\mu Re_{\text{cr}}}{\rho_{\text{air}} U_\infty c} \tag{50}$$

where, μ is the dynamic viscosity and U_∞ is the freestream velocity.

Using the Blasius laminar flow equation and the Prandtl - von Karman turbulent flow equation for skin friction on flat plates, one can weight the skin friction based on the portion of the airfoil that is taken up by laminar and turbulent flow such that

$$\begin{aligned} C_{f_{\text{lam}}} &= \frac{1.328}{\sqrt{Re}}, \\ C_{f_{\text{turb}}} &= \frac{0.455}{\log(Re)^{2.58}(1 + 0.144Ma^2)^{0.65}} \\ C_{f_c} &= x_{\text{cr}} C_{f_{\text{lam}}} + (1 - x_{\text{cr}}) C_{f_{\text{turb}}} \end{aligned} \tag{51}$$

The Reynolds number used in equation (51) to determine the skin friction is derived using the expression

$$Re = \min\left(\frac{\rho U_\infty c}{\mu}, 38.21 \frac{l}{k}^{1.053}\right) \tag{52}$$

where k is the skin roughness value which is assumed to be 0.634×10^{-5} and l is the characteristic length, which can be for example the chord or the fuselage length.

The form factor equation for the wing sections follows as

$$FF_c = \left(1 + \frac{0.6}{(x/c)_m}\frac{t}{c} + 100\left(\frac{t}{c}\right)^4\right)\left(1.34 M_\infty^{0.18} cos(\Lambda)^{0.28}\right) \tag{53}$$

where, $(x/c)_m$ and t/c are the location and thickness, respectively, at the point of maximum thickness of the airfoil.

The form factor equation for the fuselage body is taken as

$$FF_c = 1 + \frac{60}{(F_L/F_D)^3} + \frac{F_L}{400 F_D} \tag{54}$$

where F_L and F_D are the fuselage length and diameter, respectively. The flow along the fuselage is assumed to be turbulent and therefore, $x_{\text{cr}} = 0$.

Acknowledgments

The research leading to these results has received funding from the Innovate UK Agile Wing Integration Project (TSB-113041). In addition, J.E. Cooper is supported by the Royal Academy of Engineering, and S.A. Neild by EPSRC fellowship EP/K005375/1.

References

[1] Lovig, E., Downs, R., and White, E., "Passive Laminar Flow Control at Low Turbulence Levels," *AIAA Journal*, Vol. 52, No. 5, 2015.

[2] Fujino, M., Yoshizaki, Y., and Kawamura, Y., "Natural-Laminar-Flow Airfoil Development for a Lightweight Business Jet," *Journal of Aircraft*, Vol. 40, No. 4, 2003.

[3] Gregory, M., and Walker, W., "Experiments on the Use of Suction through perforated Strips for Maintaining Laminar Flow: Transition and Drag Measurements," Tech. rep., A.R.C., R. and M. 3083, 1953.

[4] Maddalon, M., and Braslow, A., "Simulated airline service flight tests of laminar-flow control with perforated-surface suction system," Tech. rep., 1990. NASA TP, 2966.

[5] Kroo, I., "DRAG DUE TO LIFT: Concepts for Prediction and Reduction," *Annual Review of Fluid Mechanics*, Vol. 33, 2000, pp. 587–617.

[6] Castrichini, A., Hodigere Siddaramaiah, V., Calderon, J., D.E.and Cooper, Wilson, T., and Lemmens, Y., "Nonlinear Folding Wing Tips for Gust Load Alleviation," *Journal of Aircraft*, Vol. 47, No. 5, 2016.

[7] Geradin, M., and Cardona, A., *Flexible Multibody Dynamics, A Finite Element Approach*, Wiley, Chichester, England, U.K., 2001.

[8] Su, W., and Cesnik, C., "Nonlinear Aeroelasticity of a Very Flexible Blended-Wing-Body Aircraft," *Journal of Aircraft*, Vol. 47, No. 5, 2010.

[9] Hodges, D., "A Mixed Variational Formulation Based on Exact Intrinsic Equations for Dynamics of Moving Beams," *International Journal of Solids and Structures*, Vol. 26, No. 11, 1990.

[10] Howcroft, C., Calderon, D., Lambert, L., Castellini, M., Cooper, J. E., Lowenberg, M., and Neild, S. A., "Aeroelastic Modelling of Highly Flexible Wings," 15th Dynamics Specialists Conference, 2016. AIAA-2016-1798.

[11] Haghighat, S., Martins, J. R. R. A., and Liu, H. H. T., "Aeroservoelastic Design Optimization of a Flexible Wing," *Journal of Aircraft*, Vol. 49, No. 2, 2012, pp. 432–443.

[12] Cur, O., Bhatia, J., Schetz, J. A., Mason, W. H., and Kapania, R. K., "Design Optimization of a Truss-Braced Wing Transonic Transport Aircraft," *Journal of Aircraft*, Vol. 47, No. 6, 2010, pp. 1907–1917.

[13] Wakayama, S., and Kroo, I., "Subsonic Wing Planform Design using Multidisciplinary Optimization," *Journal of Aircraft*, Vol. 32, No. 4, 1995.

[14] Cavagna, L., Ricci, S., and Travaglini, L., "Aeroelastic Analysis and Optimization at Conceptual Design Level Using NeoCASS Suite," 2011. AIAA 2011-2079.

[15] Cavagna, L., Ricci, S., and Riccobene, L., "A Fast Tool for Structural Sizing, Aeroelastic Analysis and Optimisation in Aircraft Coneceptual Design," 2009. AIAA 2009-2571.

[16] Torenbeek, E., "Development and Application of a Comprehensive, Design-sensitive Weight Prediction Method for Wing Structures of Transport Category Aircraft," Tech. rep., Delft University of Technology, 1992. Report LR-693.

[17] Ghiringhelli, G. L., Masarati, P., and Mantegazza, P., "Multibody Implementation of Finite Volume C0 Beams," *AIAA Journal*, Vol. 38, No. 1, 2000, pp. 131–138.

[18] Cook, R., Calderon, D., Lowenberg, M. H., Neild, S., Cooper, J. E., and Coetzee, E. B., "Worst Case Gust Prediction of Highly Flexible Wings," 58th AIAA/ASCE/AHS/ASC Structures, Structural Dynamics, and Materials Conference, 2017. AIAA-2016-1798.

[19] Masarati, P., and Mantegazza, P., "On the C0 Discretisation of Beams by Finite Elements and Finite Volumes," *l'Aerotecnica Missili e Spazio*, Vol. 75, 1995, pp. 77–86.

[20] Katz, J., and Plotkin, A., *Low Speed Aerodynamics*, 2001. Tech. Note 2249.

[21] Raymer, *Aircraft Design: A Conceptual Approach*, 5th ed., American Institute of Aeronautics and Astronautics, Inc., 2012.

[22] Bradley, M. K., Droney, C. K., and Allen, T. J., "Subsonic ultra green aircraft research: Phase II - Volume I - Truss Braced Wing Design Exploration," Tech. Rep. NASA/CR-2015-218704, 2015.

[23] Bradley, M. K., and Droney, C. K., "Subsonic ultra green aircraft research," Tech. Rep. NASA/CR-2011-216847, 2011.

[24] Castellani, M., Cooper, J., and Lemmens, Y., "Flight Loads Prediciton of High Aspect Ratio Wing Aircraft Using Multibody Dynamics," *International Journal of Aerospace Engineering*, 2016. Article 4805817.

[25] Connelly, J., and Huston, R., "The Dynamics of Flexible Multibody Systems: a Finite Segment Approach - I. Theoretical Aspects," *Computers and Structures*, Vol. 50, No. 2, 1994, pp. 225–258.

[26] Niu, M., *Airframe Stress Analysis and Sizing*, 3rd ed., Hong Kong Conmilit Press Limited, 2011.